Astrophysical S factor of $^3\mathrm{He}(\alpha,\gamma)^7\mathrm{Be}$

A. Kontos,[1,2,*] E. Uberseder,[1] R. deBoer,[1] J. Görres,[1] C. Akers,[1,3,†] A. Best,[1,‡] M. Couder,[1] and M. Wiescher[1]

[1]*Department of Physics, University of Notre Dame, Notre Dame, Indiana 46556, USA*

[2]*The Joint Institute for Nuclear Astrophysics, National Superconducting Cyclotron Laboratory,*
Michigan State University, East Lansing, Michigan 48823, USA

[3]*Department of Physics, University of Surrey, Guildford, Surrey, England*

Background: The $^3\mathrm{He}(\alpha,\gamma)^7\mathrm{Be}$ reaction is important for the neutrino production in the sun's core and the production of $^7\mathrm{Li}$ during big bang nucleosynthesis. The reaction mechanism is characterized by a strong direct capture component and nearby broad unbound resonance levels.

Purpose: Recent experiments have opened up a new energy window into the reaction mechanism and it becomes more and more evident that, in order to understand the shape of the S factor, theoretical calculations need to take into account possible resonance contributions from higher energies as well.

Method: In the present work, a relatively wide energy window was investigated, $E_{c.m.} = 300$–1460 keV, by detecting the prompt γ rays from the reaction. An extensive R-matrix analysis was performed, utilizing all modern literature capture data, as well as elastic scattering data, which are important in constraining some R-matrix parameters.

Results: The new experimental data agree very well with the modern literature data. The final result from the R-matrix fit gives a zero-energy S factor of $S(0) = 0.554(20)$ keV b. A table with the newly calculated reaction rate is given.

Conclusions: The simultaneous R-matrix analysis of the $^3\mathrm{He}(\alpha,\gamma)^7\mathrm{Be}$ and $^3\mathrm{He}(\alpha,\alpha)^3\mathrm{He}$ channels yielded a reliable fit, consistent with all the included experimental data sets. In order to further constrain the reaction rate within the R-matrix framework, additional high-energy capture data, γ-ray angular distributions, and the inclusion of other relevant reaction channels are necessary.

PACS number(s): 26.35.+c, 26.65.+t, 25.10.+s, 25.40.Lw

I. INTRODUCTION

Big bang nucleosynthesis is initiated by $p + n$ fusion one second after the big bang. It defines the abundances of the primordial isotopes, mostly hydrogen and helium, that later provide the seed for the nucleosynthesis in the first generation of stars. Big bang nucleosynthesis (BBN) calculations agree very well with abundance observations in old stars apart from the abundance of $^7\mathrm{Li}$, which the models overproduce by a factor of 3 (see [1] and references therein). The most crucial reaction that governs the production of $^7\mathrm{Li}$ is $^3\mathrm{He}(\alpha,\gamma)^7\mathrm{Be}(\beta^-, \nu)^7\mathrm{Li}$ (Gamow energy window $E_G \sim 180$ to 400 keV). The rate of this reaction is known well enough that it is unlikely that it would solve this so called *lithium problem*. However, by reducing the $^7\mathrm{Li}$ abundance uncertainty of the BBN prediction, we provide strong constrains for the proposed solutions to this problem, which might even include physics beyond the standard model.

In addition, with the construction of larger and more efficient neutrino detectors, sensitive to a wider neutrino energy range, it has become possible to detect neutrinos coming directly from the sun's core. These neutrinos are produced by the pp chain and the CNO cycle reactions. A simulated solar neutrino spectrum is shown in Fig. 1, by Bahcall and Serenelli [2].

The reaction $^3\mathrm{He}(\alpha,\gamma)^7\mathrm{Be}$ opens two important branches in the pp chains ($E_G \sim 22$ keV), which are responsible for the production of $^7\mathrm{Be}$ and $^8\mathrm{B}$ solar neutrinos (see Fig. 1). Understanding well the production of $^7\mathrm{Be}$ and $^8\mathrm{B}$ neutrinos would help to test solar models and provide a measure of the core temperature in the sun due to the strong energy dependence of reaction rates. A large fraction of the quoted uncertainty in the $^7\mathrm{Be}$ and $^8\mathrm{B}$ neutrino fluxes (10.5% and 16% respectively) arises from the uncertainty in the rate of this reaction.

Several measurements of the $^3\mathrm{He}(\alpha,\gamma)^7\mathrm{Be}$ reaction cross section (Q value = 1.587 keV) have been performed in the past [3–9]. The results have been extensively discussed in previous works and summarized by Adelberger *et al.* [10,11] and by Cyburt and Davids [12]. Because of the systematic discrepancies in the earlier results, only data from works after 2004 are taken into account in the present analysis. The experimental methods that have been used are the detection of prompt γ rays [5–8], the measurement of the $^7\mathrm{Be}$ activity [3–9], and the direct detection of the $^7\mathrm{Be}$ recoils with a recoil mass separator (Di Leva *et al.* [8]). The latter measurement extended the energy region of the available data up to $E_{c.m.} = 3.2$ MeV, providing additional constraints for models that are expected to be valid even at these energies.

Theoretical calculations by Kajino *et al.* [13] (resonating group calculation) and Descouvemont *et al.* [14] (R-matrix

---

*kontos@nscl.msu.edu

†Present address: Department of Physics, University of York, York YO10 5DD, UK and TRIUMF, Vancouver, British Columbia V6T 2A3, Canada.

‡Present address: Lawrence Berkeley National Laboratory, Berkeley, California 94720, USA.
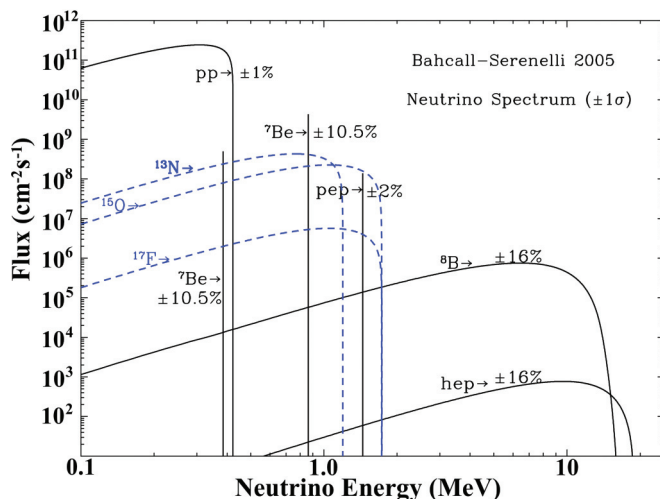
FIG. 1. (Color online) Simulated solar neutrino spectrum from the paper by Bahcall and Serenelli [2]. The continuous black lines correspond to neutrinos produced in the *pp* chains, whereas the dashed blue lines correspond to contributions of solar neutrinos originating from the CNO cycle. The continuous regions arise from the three-body kinematics of the respective decays.
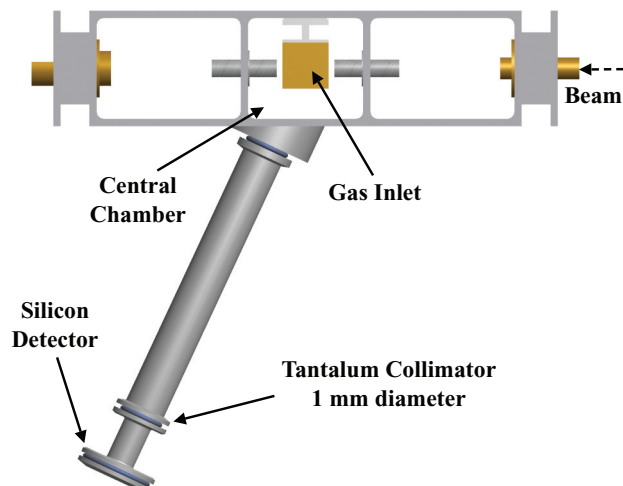

FIG. 2. (Color online) Top view of the elastic scattering set-up. The silicon detector is placed 65° from the beam axis, approximately 30 cm from the jet. The geometry is such that the silicon detector is able to detect elastically scattered particles from any point inside the central chamber.

analysis) do not describe the region at higher energies very well. On the other hand, an *ab initio* calculation by Neff [15] describes reasonably well both the capture data and the scattering phase shifts. One important conclusion in [15] is that there seems to be a significant contribution to the cross section from the internal part of the nucleus even at low energies, and therefore the reaction should not be considered purely external (e.g., as was considered in Ref. [16,17]).

In the present paper, we present a new measurement of the $^3\mathrm{He}(\alpha,\gamma)^7\mathrm{Be}$ reaction cross section with the prompt γ-ray detection method, using a helium jet gas target system. In addition, we present an updated R-matrix analysis, where both the capture and scattering channels are fitted simultaneously, over a wide energy range. A table with the newly calculated reaction rate is given.

II. EXPERIMENTAL SETUP AND PROCEDURE

The experiments were carried out at the Nuclear Science Laboratory at the University of Notre Dame. A $^3\mathrm{He}$ beam was provided by the 4 MV KN Van de Graaff accelerator covering the energy range $E_{^3\mathrm{He}} = 530$–2550 keV ($E_{c.m.} = 300$–1460 keV). Typical beam currents between 10 and 20 p μA were achieved with a beam energy resolution of approximately 3.0 keV and an energy uncertainty of 1.0 keV. The $^3\mathrm{He}$ beam was guided and focused by a series of optical elements on the windowless supersonic helium gas jet target HIPPO. For a detailed description of the properties and experimental characterization of HIPPO the reader is directed to [18]. The spatial profile of the helium jet is Gaussian with 2.2 ± 0.2 mm full width at half maximum and a peak target thickness of $(2.6 \pm 0.2) \times 10^{17}$ atoms/cm^2.

The main chamber of the gas target system is shown in Fig. 2. The nozzle is placed vertically with the jet flowing

downwards. The beam enters from the right through a series of cylindrical apertures that separate one pumping stage from the next. With the use of electrostatic steerers the beam is tuned at the center of the jet. The overlap of the beam particles with the jet is continuously monitored by a silicon detector placed at 65° relative to the beam axis at a distance of approximately 30 cm from the jet area. A 1 mm tantalum collimator located 3.0 cm from the detector reduced the count rate and reduced multiple scattering events from the walls of the setup. Due to the small dimensions of the jet, all the interaction region is being monitored by the silicon detector, which is necessary for the normalization of the data. The beam exits the main chamber to the left again through a series of cylindrical apertures and is stopped about 1 meter downstream on a tantalum backing in order to minimize beam-induced background reactions.

A 50% high-purity Ge (HPGe) detector was placed at 90° relative to the beam axis and as close to the jet as possible, as shown in Fig. 3. An important feature of the gas target system is its particularly compact design which maximizes γ-ray detection efficiency around the target. The distance between the front edge of the germanium detector and the jet was around 5 cm. The thickness of the main chamber's wall is 5 mm. The HPGe detector was surrounded by a lead castle to reduce room background radiation (5–10 cm thickness). The second HPGe detector shown in the figure was used only for beam-energy calibration purposes.

For the absolute cross section measurement of the $^3\mathrm{He}(\alpha,\gamma)^7\mathrm{Be}$ reaction, it was necessary to accurately determine the solid and polar angle of the silicon detector and the absolute peak efficiency of the germanium detector. The solid angle of the silicon detector was measured with a calibrated mixed alpha source ($^{148}\mathrm{Gd}$, $^{241}\mathrm{Am}$) placed at the position of the jet. The result was $\Omega_{source} = (8.99 \pm 0.13) \times 10^{-6}$ sr, in agreement with the calculated solid angle from the geometry.
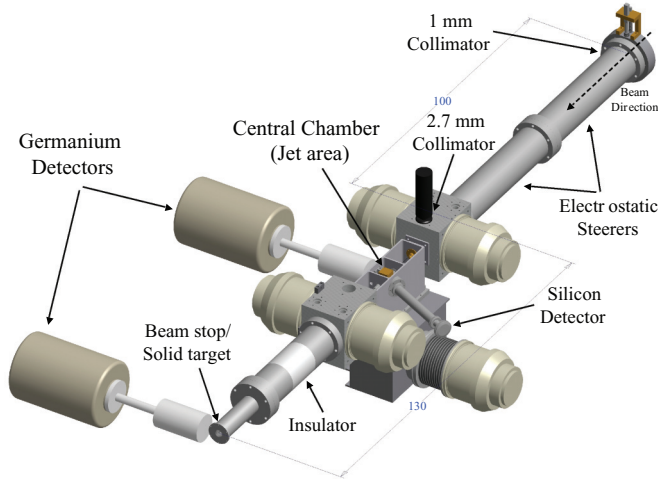
FIG. 3. (Color online) Experimental setup. The germanium detector at the end of the beamline (beam stop) was used for beam-energy calibration purposes. The indicated distances are in mm.

The uncertainty includes the uncertainty from the counting statistics and the uncertainty in the source's activity.

The polar angle of the silicon detector was determined from the measured yield ratio of the detected ^{3}He and ^{4}He particles.[1] A typical Si-detector spectrum of the two particle peaks is shown in Fig. 4. The elastic scattering cross section, which is needed for the normalization of the data, was obtained from the *R*-matrix analysis of elastic scattering literature data [19,20], and is discussed in a following section. The result from this measurement was an angle value of $64.8° \pm 0.3°$ in the laboratory reference frame, consistent with the mechanical design. The error arises mainly from the uncertainty of the elastic scattering cross section.

_____

[1] At this angle and beam-to-target mass ratio, the detector records scattered particles both from the beam and from the target.
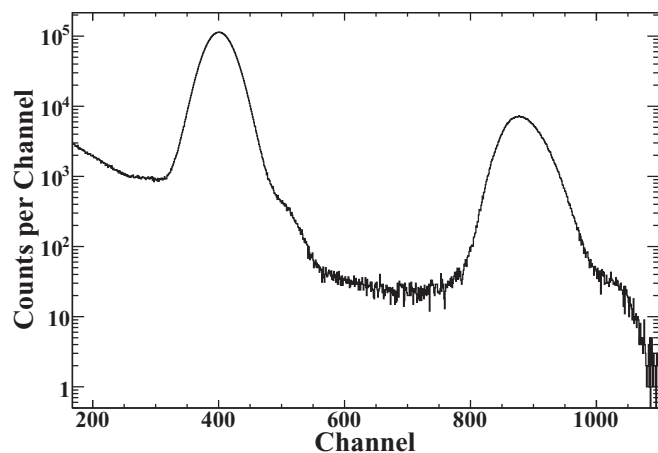

FIG. 4. Silicon detector spectrum at $E_{c.m.} = 1$ MeV. The low-energy peak corresponds to scattered ^{4}He nuclei from the jet, and the higher-energy peak corresponds to the scattered ^{3}He beam.

The absolute peak efficiency of the germanium detector was measured with the calibrated γ sources, ^{22}Na, ^{60}Co, ^{133}Ba, and ^{137}Cs. A relative efficiency curve was obtained with the narrow resonance of the ^{14}N$(\alpha,\gamma)^{18}$F reaction at 1620 keV [21], and was used to constrain the energy dependence of the curve in the higher energy region. Figure 5 shows the result of the peak efficiency measurements along with the fit obtained (solid line) for a third-order logarithmic polynomial ($\chi^2/\nu = 1.3$). The uncertainty of the peak efficiency was 6%, and it arises from a 3% uncertainty in the activity of the sources, a 5% uncertainty in the normalization factor for ^{14}N$(\alpha,\gamma)^{18}$F, and a 2% statistical error.

Coincidence summing corrections for both the efficiency and the cross section measurements were calculated from the branching ratio information and the total efficiency of the detector. The latter was measured at $E_\gamma = 661$ and 1252 keV with two calibrated γ sources, ^{60}Co and ^{137}Cs. GEANT4 simulations [22], normalized to these two data points, were used to extrapolate to the entire energy range of interest. The uncertainty of the total efficiency was 10%. The coincidence summing corrections were of the order of 5% for the 429 keV γ ray.

In addition, the efficiency was measured as a function of the source position along the beam axis, in between the apertures. The reason for this measurement was to test whether the γ-ray yield required any corrections due to the finite size of the helium jet. The measurement showed no correlation between γ-ray yield and the position of the source, which indicated that no correction was needed.

The radiative capture cross section can be experimentally determined using the formula

$$\sigma_{fusion} = \frac{N(E_\gamma, \theta)}{N_{target} N_{proj} \eta_{pe}(E_\gamma) B(E_\gamma) W(E_\gamma, \theta)}, \quad (1)$$

where $N(E_\gamma, \theta)$ is the number of γ rays detected at a particular energy of interest, θ the angle of the detector, N_{target} the average thickness of the helium jet as seen by the beam (in atoms/cm^2), N_{proj} the total number of ^{3}He atoms in each run, $\eta_{pe}(E_\gamma)$ the γ-ray peak efficiency and $B(E_\gamma)$ the branching ratio of the detected γ ray. $W(E_\gamma, \theta)$ is the correction associated with the angular distribution of
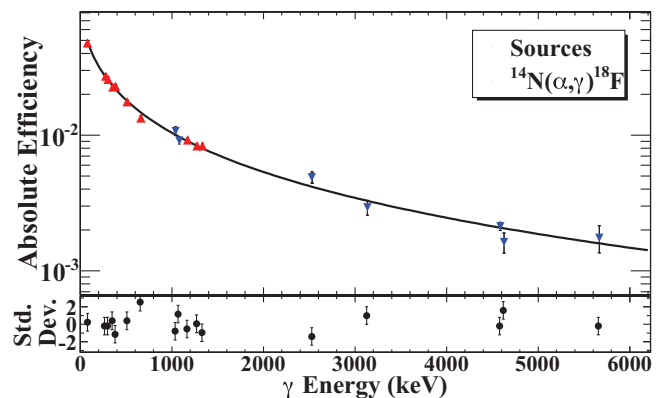

FIG. 5. (Color online) Peak γ-ray detection efficiency of the gas target setup.

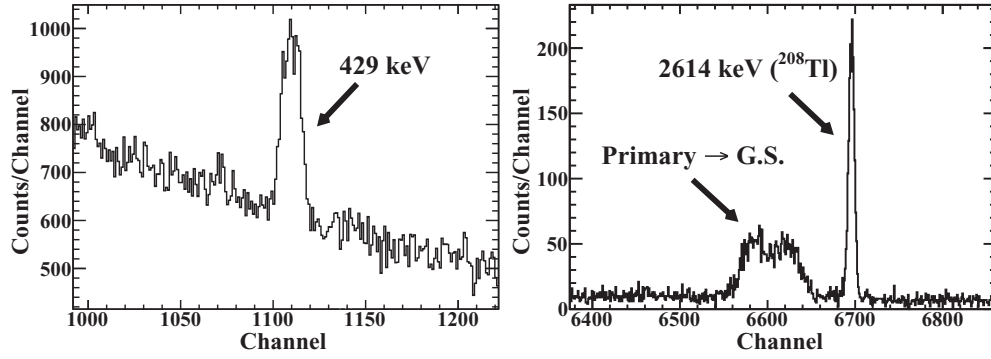FIG. 6. γ-ray spectrum of the experiment at $E_{c.m.} = 1$ MeV, showing the two main peaks of interest. The left-hand side of the figure shows the 429 keV γ line and the right-hand side the primary transition to the ground state ($E_\gamma = 2.59$ MeV). The broad γ peak of the ground state transition is due to the Doppler effect.

the γ-rays of interest and the finite size of the γ-ray detector. The secondary transition from the first excited to the ground state is isotropic, whereas for the primary transition to the ground state, the angular distribution was determined from the R-matrix analysis. The correction amounted to less than 2%.

The product $N_{target} \times N_{proj}$ in Eq. (1) was measured online using the ^{3}He and ^{4}He silicon detector yields using the equation

$$N_{target} \times N_{proj} = \frac{N_{He}}{\left(\frac{d\sigma}{d\Omega}\right)_{el}\Omega_{Si}}, \qquad (2)$$

where N_{He} is the number of ^{3}He or ^{4}He counts, Ω_{Si} is the solid angle of the silicon detector, and $(\frac{d\sigma}{d\Omega})_{el}$ is the elastic scattering cross section, as obtained from the R-matrix analysis of scattering data (see Sec. III). In this way, the overlap of the beam with the jet was monitored constantly and was used for the normalization of the data. The uncertainty in the product was approximately 5% and arises mainly from the uncertainty in the elastic scattering cross section. It should be noted that no corrections were made that were related to beam heating effects, as they have been shown to be negligible for jet gas targets for similar conditions [23].

With this method of normalization, it was important to exclude the possibility that a fraction of the scattered nuclei are deflected away from the silicon detector by interacting with the helium jet and the ambient gas around it. GEANT simulations showed that the effect of the gas to the trajectory of the scattered nuclei is negligible and therefore no corrections were required.

Figure 6 shows a γ-ray spectrum at $E_{c.m.} = 1$ MeV. The primary transition to the ground state ($E_\gamma = 2.59$ MeV) is shown in the right-hand side of the figure. The left-hand side of the figure shows the 429 keV γ line, which results from the population of the first excited state of ^{7}Be and its subsequent deexcitation. The γ line from the primary transition to the first excited state (not shown in the figure) was not considered in the analysis, since the latter was much harder to distinguish, due to its lower intensity and the larger background coming from the Compton continuum from the transition to the ground state, as well as other background lines.

Beam induced background from the aluminum apertures was reduced to a minimum by carefully tuning the beam

through them. However, even with good tuning, some background γ rays were observed. The most prominent one was the 511 keV annihilation γ-ray line, which was the main contributor to the background below the 429 keV γ ray. The Doppler shift observed for both γ lines of interest, and especially for the ground state primary transition is due to the close detection geometry and the comparable masses of the interacting particles.

The final results are summarized in Fig. 7 and Table I. For comparison, Fig. 7 includes all available data from experimental efforts after 2004. The present data (black full circles) are found to be in agreement with previous measurements. The data are presented with their respective total experimental

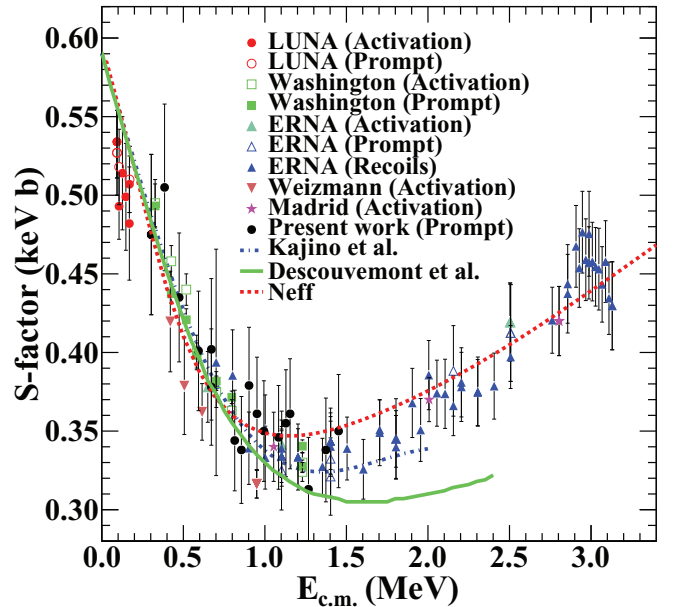FIG. 7. (Color online) Comparison of the total S factor result obtained from the present experiment with previous data. The data on the graph include total uncertainties. Very good agreement with the previous data sets is observed. The calculations by Kajino *et al.* [13] and Descouvemont *et al.* [14] have been normalized to the $S(0)$ value of Neff [15], to allow for a comparison of the S-factor shapes.

TABLE I. Experimental S factor and branching ratio of ^{4}He(^{3}He,γ)^{7}Be.

$E_{c.m.}$ (keV)	S factor (keV b)[a]	γ_{429}/γ_0 ($\times 10^{-2}$)
303.4	$0.475 \pm 0.033 \pm 0.038$	44 ± 8
384.9	$0.505 \pm 0.034 \pm 0.041$	41 ± 7
474.2	$0.435 \pm 0.021 \pm 0.035$	39 ± 5
593.1	$0.401 \pm 0.020 \pm 0.032$	35 ± 4
671.7	$0.378 \pm 0.021 \pm 0.031$	40 ± 5
671.8	$0.402 \pm 0.032 \pm 0.032$	39 ± 7
815.0	$0.344 \pm 0.016 \pm 0.028$	34 ± 4
856.0	$0.338 \pm 0.020 \pm 0.027$	42 ± 6
902.8	$0.379 \pm 0.021 \pm 0.031$	36 ± 5
951.6	$0.361 \pm 0.021 \pm 0.029$	42 ± 5
994.0	$0.350 \pm 0.015 \pm 0.028$	40 ± 4
1084.0	$0.346 \pm 0.017 \pm 0.028$	42 ± 5
1129.0	$0.355 \pm 0.018 \pm 0.029$	36 ± 4
1154.5	$0.361 \pm 0.019 \pm 0.029$	41 ± 5
1267.4	$0.313 \pm 0.022 \pm 0.025$	36 ± 6
1374.1	$0.338 \pm 0.018 \pm 0.027$	45 ± 6
1452.0	$0.350 \pm 0.023 \pm 0.028$	35 ± 6

[a]The reported uncertainties correspond to the statistical and systematic uncertainties, respectively.

uncertainties. The total systematic uncertainty of the present measurement is estimated to be 8% with contributions from: 6% uncertainty in the peak efficiency, 2% in the silicon detector efficiency, and 5% uncertainty in the elastic scattering cross section. Measurements at higher energies were inhibited by high beam induced background levels. At lower energies the limiting factor was the very low γ-ray yield.

Also shown in Fig. 7 are previous theoretical attempts to describe the reaction cross section. From the three works shown here, the calculations from Kajino *et al*. [13] and Descouvemont *et al*. [14] require normalization to the available capture data, whereas the *ab initio* calculation by Neff [15] does not. To allow for a comparison of the S-factor shapes, the calculations by Kajino *et al*. and Descouvemont *et al*. have been normalized to the $S(0)$ value of Neff. The best description of the entire energy range is achieved by Neff, whose model also reproduces the scattering phase shifts. In the following sections, we attempt to obtain a good description of all the data using a phenomenological R-matrix analysis, including both the capture and scattering channels [24].

The ratio γ_{429}/γ_0 is reported in Table I as a function of energy. No energy dependence is observed for the ratio, within the sensitivity of this experiment. The uncertainties are mostly due to the large uncertainty in determining the background of the 429 keV line. No significant discrepancy from previous measurements is observed.

III. *R*-MATRIX ANALYSIS AND DISCUSSION

A multichannel, multilevel R-matrix analysis was performed using the techniques outlined in Ref. [24]. The analysis simultaneously included all the capture data shown in Fig. 7 (123 experimental points) as well as ^{3}He(α,α)^{3}He scattering data from [19,20] (698 experimental points). These particular

TABLE II. Data set normalization factors.

Data set	Quoted sys. uncertainty	Normalization
Barnard *et al*. (Elastic) [20]	5%	1.033
Mohr *et al*. (Elastic) [19]	5%[a]	1.020
LUNA (Activation) [4,5]	3.2%	1.013
LUNA (Prompt) [5]	3.8%	1.002
Washington (Activation) [6]	3.0%	0.980
Washington (Prompt) [6]	3.5%	0.975
ERNA (Activation) [8]	5.0%	0.973
ERNA (Prompt) [8]	7.0%	0.986
ERNA (Recoils) [8]	5.0%	0.982
Weizmann (Activation) [3]	3.7%	1.063
Madrid (Aactivation) [9]	3.0%	0.976
Notre Dame (Prompt)	8.0%	0.970
Capture average		0.993

[a]The uncertainty for this data set was assumed to be the same as that of the other scattering experiment, since there is no mention on uncertainties in the paper.

scattering data sets were chosen because they cover the same ^{7}Be excitation energy range as the capture data. The systematic uncertainties of the data sets were taken into account in the fitting algorithm, by adding a corresponding term in the χ^2 formula and allowing the normalization of the data sets to vary according to their systematic uncertainty, as described in [25]. A table with the resulting normalization factors is given at the end of this section (Table II). Correlations among systematic uncertainties were not considered.

For the best description of the elastic scattering data, the present R-matrix analysis included hard sphere scattering up to $L = 5$, the well known level at 4.56 MeV $7/2^-$, and seven background poles with orbital angular momenta up to $l = 3$. Six of these background poles were placed at 11 MeV of excitation energy of ^{7}Be, with $J^\pi = 0.5^+, 0.5^-, 1.5^-, 1.5^+, 2.5^+$, and 3.5^-, and one at 7 MeV, with $J^\pi = 2.5^-$. Placing the latter background pole at higher energies resulted in unphysically large α widths, as it was trying to compensate for observed levels below 10 MeV [26]. Neither the χ^2 nor the S factor depends significantly on the inclusion of more background poles or the choice of their exact energy, as long as their excitation energy is higher than 10 MeV, with the exception of the 7 MeV pole. However, fits with higher energy background poles resulted in disproportionately higher α widths, relative to the increase of the penetrability.

The external capture calculation included $E1$, $M1$, and $E2$ components.[2] The ANC values of the ground and first excited states were free fit parameters in the R-matrix analysis. Only $E1$ transitions of background poles were considered in order to minimize the number of free parameters. The total number of free R-matrix parameters was 17. The channel radius was taken as $r_c = 4.6$ fm, just large enough to ensure minimum

[2]The $E1$ transition dominates in most of the energy range, but there was no reason to exclude the other two from the calculations.
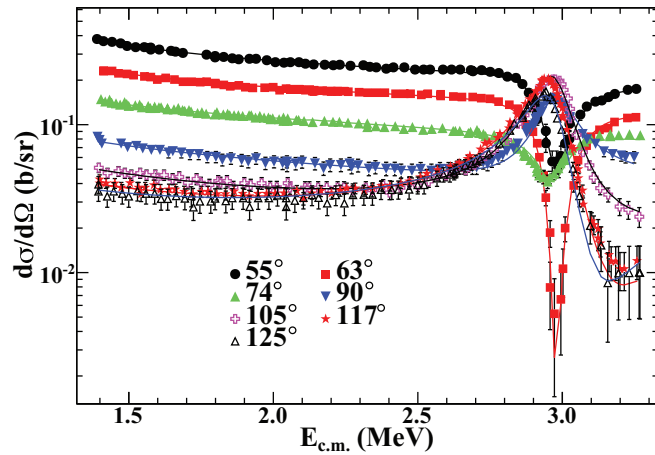
FIG. 8. (Color online) *R*-matrix fit of ^{3}He$(\alpha, \alpha)^3$He data from [20]. The energies and angles are in the center-of-mass frame. The error bars on the figure correspond to the inflated statistical uncertainties.

nuclear interaction between the channel nuclei.[3] Just as with the background pole energies, the fit was insensitive to the value of the channel radius as long as $r_c \geqslant 4.0$ fm. More specifically, the $S(0)$ value varied by approximately 0.5% for channel radii $4.0 < r_c < 5.0$ fm.

Figure 8 shows the result for the elastic scattering data of Barnard *et al.* [20], as was obtained by the simultaneous *R*-matrix fit. The data set of [19] is also described reasonably well. The statistical uncertainties were inflated by a constant factor so as to obtain a reduced χ^2 of 1 for each of the two scattering data sets.

The result for the capture channel, as obtained from the simultaneous *R*-matrix analysis, is shown with the black thick continuous lines in Figs. 9 and 10. Figure 9 shows the result of the total capture *S* factor, whereas Fig. 10 shows the individual contributions to the total capture from the ground and first excited states of ^{7}Be. Experimental data are also plotted for comparison. Note that the data sets on the figures are normalized by the fitting algorithm as discussed at the beginning of the section. The resulting zero-energy *S* factor from the fit is $S(0) = 0.554$ keV b. The calculation reproduces the data very well. The Washington prompt data especially fall well within the present calculation, despite their small statistical uncertainties. The agreement is also clear in Fig. 10. In addition, it is interesting that this calculation reproduces the seemingly low *S* factor of the LUNA measurements and the high-energy data. The resulting normalization factors for each data set are listed in Table II, along with the corresponding systematic uncertainties for comparison. As expected, the normalization factors did not deviate from unity much more than the systematic uncertainty allows, with the exception
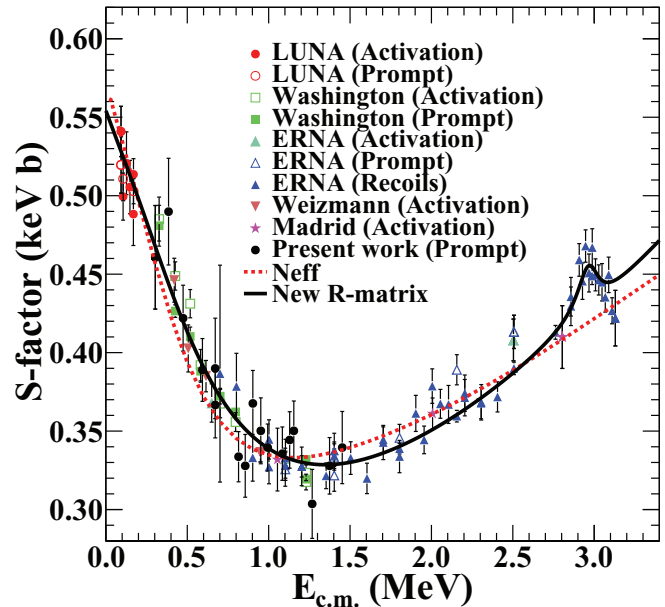

FIG. 9. (Color online) Comparison of present *R*-matrix fit (black continuous line) to the experimental data. The data sets have been normalized according to Table II. The error bars on the figure correspond to statistical uncertainties only, unlike those shown in Fig. 7. The calculation by Neff [15] is also shown, arbitrarily normalized to make the comparison easier. The shape of the calculated *S* factor is in very good agreement with the experimental shape.

of the Weizmann data set which required a 6% correction compared to the reported 3.7% systematic uncertainty.

The reduced χ^2 of the capture data was $\chi^2/\nu = 1.4$. The uncertainty in the final $S(0)$ value arises from the choice of channel radius r_c and the position of the background poles (1.0%), and from how well the data with their respective total uncertainties constrain the fit (3.5%). The latter uncertainty estimate was calculated with the MINOS method of MINUIT2
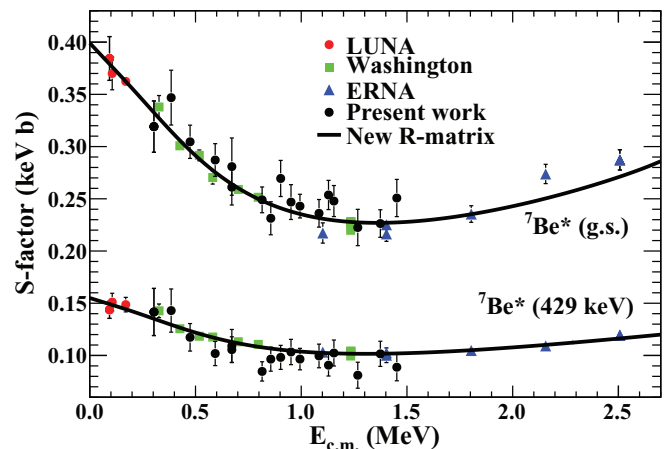
FIG. 10. (Color online) Comparison of present *R*-matrix fit (black continuous line) to the experimental prompt γ-ray data for the two ^{7}Be final states. The error bars on the figure correspond to statistical uncertainties only.

---

[3]Assuming uniform nuclear density distribution and taking into account the measured rms charged radii of ^{3}He ($r_{rms} = 1.96$ fm [27]) and ^{4}He ($r_{rms} = 1.67$ fm [28]), the minimum distance can be calculated as $r_c = \sqrt{5/3}(1.96 + 1.67) \sim 4.7$ fm.

TABLE III. R-matrix best fit parameters ($r_c = 4.6$ fm).

E_x	J^π	l	Γ_W[a] (MeV)	Γ_α (MeV)	$\Gamma_\gamma(0)$ (keV)	$\Gamma_\gamma(429)$ (keV)
11	0.5^+	0	13.1	16.6	-0.61[b]	0.66
11	0.5^-	1	12.3	6.1		
11	1.5^+	2	10.5	15.9	-0.34[b]	0.07
11	1.5^-	1	12.3	13.3		
11	2.5^+	2	10.5	9.4	-0.03[b]	
7	2.5^-	3	3.2	2.9		
4.56	3.5^-	3		0.157	36×10^{-6}	
11	3.5^-	3	7.7	11.5		
ANC(0) = 4.0 fm$^{-1/2}$				ANC(429) = 3.1 fm$^{-1/2}$		

[a]Γ_W is the α width derived from the Wigner limit, calculated from the equation $\Gamma_W = 2P\gamma_W^2$, where P is the penetrability and $\gamma_W^2 = (3/2)\hbar^2/(\mu r_c^2)$.
[b]The negative sign on the partial width signifies the relative interferences.

[29]. The final value, $S(0) = 0.554(20)$ keV b, is lower by only 1% from a recent evaluation of the modern data [11], where $S(0) = 0.56(3)$ keV b, and 4.5% lower from the evaluation by Cyburt and Davids [12], where $S(0) = 0.580(43)$ keV b. To understand the model uncertainty of the reaction better, we compared the shape of the present calculation with the calculations by Kajino *et al.* [13], Descouvemont *et al.* [14], and Neff [15]. A maximum of 4% deviation between models is observed in the energy range $E_{c.m.} = 0$–1.0 MeV. Only the latter comparison is shown in Fig. 9 for clarity.

The final R-matrix parameters are listed in Table III. For comparison, the table also lists values of particle widths derived from the Wigner limit, calculated at the background-pole energies. All background-pole widths have values lower than or close to the respective Wigner-limit widths. None of the resulting Γ_γ widths is higher than the respective Weisskopf estimate ($\sim$1.3 keV).

Additional measurements on both the scattering and capture channels, as well as the inclusion of more relevant channels in the R-matrix analysis, such as ^{6}Li + p channels, would help improve further our understanding of the reaction, in the context of the R-matrix theory.

IV. REACTION RATE

The total thermonuclear rate for the ^{3}He(α,γ)^{7}Be reaction was calculated by direct numerical integration of the formula

$$N_A \langle \sigma v \rangle = 3.7318 \times 10^{10} \mu^{-1/2} T_9^{-3/2}$$
$$\times \int_0^\infty \sigma(E) E e^{-11.605 E/T_9} dE, \qquad (3)$$

where the rate is in units of cm^{3}s^{-1}mole^{-1}, T_9 is the stellar temperature in GK, μ is the reduced mass, E is the center-of-mass energy in MeV, and $\sigma(E)$ is the reaction cross section in barns. The result of the calculation as a function of temperature is listed in Table IV. The uncertainty of the reaction rate calculation is taken to be approximately 3.5%,

TABLE IV. ^{3}He(α,γ)^{7}Be reaction rates. Rate units are in cm^{3}s^{-1}mole^{-1}.

T_9	Reaction rate	T_9	Reaction rate
0.001	1.125×10^{-47}	0.14	3.826×10^{-04}
0.002	2.203×10^{-36}	0.15	6.392×10^{-04}
0.003	6.536×10^{-31}	0.16	1.021×10^{-03}
0.004	1.836×10^{-27}	0.18	2.333×10^{-03}
0.005	5.185×10^{-25}	0.2	4.739×10^{-03}
0.006	3.826×10^{-23}	0.25	1.945×10^{-02}
0.007	1.184×10^{-21}	0.3	5.655×10^{-02}
0.008	2.007×10^{-20}	0.35	1.317×10^{-01}
0.009	2.191×10^{-19}	0.4	2.632×10^{-01}
0.01	1.715×10^{-18}	0.45	4.705×10^{-01}
0.011	1.035×10^{-17}	0.5	7.731×10^{-01}
0.012	5.079×10^{-17}	0.6	$1.739 \times 10^{+00}$
0.013	2.104×10^{-16}	0.7	$3.296 \times 10^{+00}$
0.014	7.578×10^{-16}	0.8	$5.550 \times 10^{+00}$
0.015	2.426×10^{-15}	0.9	$8.582 \times 10^{+00}$
0.016	7.028×10^{-15}	1	$1.245 \times 10^{+01}$
0.018	4.609×10^{-14}	1.25	$2.592 \times 10^{+01}$
0.02	2.325×10^{-13}	1.5	$4.490 \times 10^{+01}$
0.025	5.918×10^{-12}	1.75	$6.919 \times 10^{+01}$
0.03	6.951×10^{-11}	2	$9.847 \times 10^{+01}$
0.04	2.493×10^{-09}	2.5	$1.705 \times 10^{+02}$
0.05	3.151×10^{-08}	3	$2.585 \times 10^{+02}$
0.06	2.168×10^{-07}	3.5	$3.602 \times 10^{+02}$
0.07	1.007×10^{-06}	4	$4.742 \times 10^{+02}$
0.08	3.560×10^{-06}	5	$7.351 \times 10^{+02}$
0.09	1.033×10^{-05}	6	$1.035 \times 10^{+03}$
0.1	2.578×10^{-05}	7	$1.370 \times 10^{+03}$
0.11	5.726×10^{-05}	8	$1.738 \times 10^{+03}$
0.12	1.159×10^{-04}	9	$2.135 \times 10^{+03}$
0.13	2.173×10^{-04}	10	$2.558 \times 10^{+03}$

which is the uncertainty of the $S(0)$ from the R matrix. A comparison between this reaction rate and those by Cyburt and Davids [12], Descouvemont *et al.* [14], and Adelberger *et al.* [11] is shown in Fig. 11, where the ratios relative to [11] are plotted as a function of temperature. The rate by Adelberger *et al.* [11] was calculated from Eq. (8) found in Ref. [11], using $S(0) = 5.6 \times 10^{-4}$ MeV b, $S'(0)/S(0) = -0.64$ MeV^{-1}, and $S''(0)/S(0) = 0.27$ MeV^{-2}, as recommended in the same paper.[4] The rate by Descouvemont *et al.* is much lower than all the other rates. This is most likely because measurements up to that time were suggesting a lower S factor. For temperatures below $T_9 = 1$, the new rate is within $\sim$2% from that of Adelberger *et al.* and within approximately $\sim$4% from that of Cyburt and Davids. As we go higher in temperatures the calculations by Adelberger *et al.* and Cyburt & Davids [12] are less valid, since the former was meant only for solar fusion temperatures and at the time of the latter the high-energy data were not available. To connect the results back to the astrophysical motivation, we focus on the comparison with the rate by Cyburt and Davids, where the deviation is slightly

---

[4]The values for the derivatives used in [11] were taken from the theoretical work by Nollett [30].
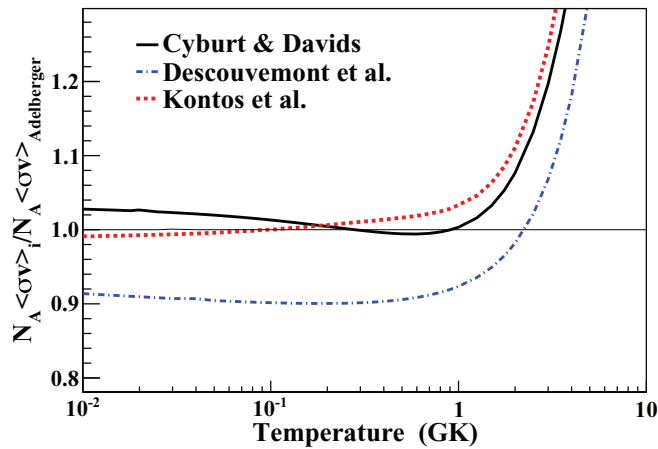
FIG. 11. (Color online) The reaction rate ratio as a function of temperature of various evaluations relative to the rate by Adelberger *et al.* [11]. The result by Cyburt and Davids [12] is shown with a black continuous line, the blue dashed-dotted line is the evaluation by Descouvemont *et al.* [14], and the result from the present work is the red dashed line.

larger. For temperatures relevant to solar neutrino production ($T_9 \lesssim 0.015$) the reaction rate is approximately 4% lower than the rate in [12]. This translates to a $\sim$3.5% and $\sim$3.3% decrease of the ^{7}Be and ^{8}B solar neutrino fluxes respectively, as can be calculated from the relations $\phi_\nu(^7Be) \propto S(0)^{0.86}$ and $\phi_\nu(^8B) \propto S(0)^{0.81}$ given in [31]. For BBN temperatures ($0.3 < T_9 < 0.8$) the current calculation is 1%–3% higher than in [12], which would increase almost proportionally the predicted ^{7}Li abundance [32]. The uncertainty from this new analysis of the reaction is 3.6%, which would lower the uncertainties of the predicted BBN ^{7}Li abundance and the related neutrino fluxes from the sun. The exact implications of this uncertainty reduction are beyond the scope of this work.

V. SUMMARY AND CONCLUSION

The fusion cross section of ^{3}He$(\alpha, \gamma)^7$Be was measured in the energy range $E_{c.m.} = 300$–1460 keV, by detecting the prompt γ-rays from the reaction. The experimental results agree very well with the literature data. To understand the shape of the S factor throughout the measured energy range, we performed an extensive R-matrix analysis of both the elastic scattering and capture channels. By including the elastic scattering data in the analysis, it was possible to constrain the particle widths of the required poles, and therefore better represent the scattering wave function. The resulting calculations were able to describe the data with high accuracy over the entire energy range available. The obtained reaction rate was found to be within the uncertainties of previous calculations. The estimated uncertainty of $S(0)$ from this new analysis is 3.6%, lower than previous evaluations. However, it is important that further work is done to include additional channels in the R-matrix analysis as well as better techniques are developed for evaluating its uncertainty. On the experimental side, future measurements should focus on obtaining accurate angular distribution data of the prompt γ rays, as this information could further constrain theoretical models. Data at even higher energies will also help with a more reliable description of the S factor.

[1] B. D. Fields, Annu. Rev. Nucl. Part. Sci. **61**, 47 (2011).

[2] J. N. Bahcall, A. M. Serenelli, and S. Basu, Astrophys. J. **621**, L85 (2005).

[3] B. S. Nara Singh, M. Hass, Y. Nir-El, and G. Haquin, Phys. Rev. Lett. **93**, 262503 (2004).

[4] Gy. Gyürky *et al.*, Phys. Rev. C **75**, 035805 (2007).

[5] F. Confortola *et al.*, Phys. Rev. C **75**, 065803 (2007).

[6] T. A. D. Brown, C. Bordeanu, K. A. Snover, D. W. Storm, D. Melconian, A. L. Sallaska, S. K. L. Sjue, and S. Triambak, Phys. Rev. C **76**, 055801 (2007).

[7] H. Constantini *et al.*, Nucl. Phys. A **814**, 144 (2008).

[8] A. Di Leva *et al.*, Phys. Rev. Lett. **102**, 232502 (2009).

[9] M. Carmona-Gallardo *et al.*, Phys. Rev. C **86**, 032801(R) (2012).

[10] E. G. Adelberger *et al.*, Rev. Mod. Phys. **70**, 1265 (1998).

[11] E. G. Adelberger *et al.*, Rev. Mod. Phys. **83**, 195 (2011).

[12] R. H. Cyburt and B. Davids, Phys. Rev. C **78**, 064614 (2008).

[13] T. Kajino, H. Toki, and S. M. Austin, Astrophys. J. **319**, 531 (1987).

[14] P. Descouvemont, A. Adahchour, C. Angulo, A. Coc, and E. Vangioni-Flam, At. Data Nucl. Data Tables **88**, 203 (2004).

[15] T. Neff, Phys. Rev. Lett. **106**, 042502 (2011).

[16] T. A. Tombrello and P. D. Parker, Phys. Rev. **130**, 1112 (1963).

[17] T. A. Tombrello and P. D. Parker, Phys. Rev. **131**, 2582 (1963).

[18] A. Kontos, D. Schürmann, C. Akers, M. Couder, J. Görres, D. Robertson, E. Stech, R. Talwar, and M. Wiescher, Nucl. Instrum. Methods A **664**, 272 (2012).

[19] P. Mohr, H. Abele, R. Zwiebel, G. Staudt, H. Krauss, H. Oberhummer, A. Denker, J. W. Hammer, and G. Wolf, Phys. Rev. C **48**, 1420 (1993).

[20] A. C. L. Barnard, C. M. Jones, and G. C. Phillips, Nucl. Phys. **50**, 629 (1964).

[21] E. A. Silverstein, S. R. Salisbury, G. Hardie, and L. D. Oppliger, Phys. Rev. **124**, 868 (1961).

[22] E. A. Silverstein, S. R. Salisbury, G. Hardie, and L. D. Oppliger (Geant4 Collaboration), Nucl. Instrum. Methods A **506**, 250 (2003).

[23] J. Görres, H. W. Becker, A. Krauss, A. Redder, C. Rolfs, and H. P. Trautvetter, Nucl. Instrum and Methods A **241**, 334 (1985).

[24] R. E. Azuma *et al.*, Phys. Rev. C **81**, 045805 (2010).

[25] G. DAgostini, Nucl. Instrum. Methods A **346**, 306 (1994).

[26] R. J. Spiger and T. A. Tombrello, Phys. Rev. **163**, 964 (1969).

[27] D. C. Morton, Q. Wu, and G. W. F. Drake, Phys. Rev. A **73**, 034502 (2006).

[28] I. Sick, Phys. Rev. C **77**, 041302(R) (2008).

[29] F. James and M. Winkler, Minuit User's Guide (2008), http://www.cern.ch/minuit.

[30] K. M. Nollett, Phys. Rev. C **63**, 054002 (2001).

[31] J. N. Bahcall and R. K. Ulrich, Rev. Mod. Phys. **60**, 297 (1988).

[32] R. H. Cyburt, Phys. Rev. D **70**, 023505 (2004).